

In vivo metallophilic self-assembly of a light-activated anticancer drug

Sylvestre Bonnet (✉ bonnet@chem.leidenuniv.nl)

Leiden University <https://orcid.org/0000-0002-5810-3657>

Xue-Quan Zhou

Leiden University

Peiyuan Wang

Fudan University

Vadde Ramu

Leiden Univeristy

Suhua Jiang

Assembly of Functional Nanostructures, Fujian Institute of Research on the Structure of Matter, Chinese Academy of Sciences

Xuezhao Li

State Key Laboratory of Fine Chemicals, Dalian University of Technology

Selda Abyar

Leiden Univeristy

Panagiota Papadopoulou

Leiden Univeristy <https://orcid.org/0000-0003-3174-6270>

Yang Shao

Leiden Univeristy

Maxime Siegler

Johns Hopkins University

Francesco Buda

Leiden Univeristy <https://orcid.org/0000-0002-7157-7654>

Alexander Kros

Leiden University <https://orcid.org/0000-0002-3983-3048>

Wen Sun

State Key Laboratory of Fine Chemicals, Dalian University of Technology

Article

Keywords:

Posted Date: January 18th, 2022

DOI: <https://doi.org/10.21203/rs.3.rs-965808/v1>

License:   This work is licensed under a Creative Commons Attribution 4.0 International License.

[Read Full License](#)

Version of Record: A version of this preprint was published at Nature Chemistry on May 11th, 2023. See the published version at <https://doi.org/10.1038/s41557-023-01199-w>.

Abstract

Self-assembling molecular drugs combine the easy preparation typical of small-molecule chemotherapy and the tumor-targeting properties of drug-nanoparticle conjugates. However, they require a supramolecular interaction that survives the complex environment of a living animal. Here, we report that the metallophilic interaction between cyclometalated palladium complexes generates supramolecular nanostructures in living mice that have a long circulation time (above 12 h) and efficient tumor accumulation rate (up to 10.2% ID/g) in a skin melanoma tumor model. Green light activation leads to efficient tumor destruction due to the photodynamic effect generated by the self-assembled palladium complexes, as demonstrated *in vitro* by an up to >96-fold cytotoxicity increase upon irradiation. This work demonstrates that metallophilic interactions are well suited for generating stable supramolecular nanotherapeutics *in vivo* with exceptional tumor-targeting properties.

Main Text

Curing cancer is one of the toughest challenges of modern medicine,¹ and chemotherapy occupies the front line of cancer treatment.²⁻⁴ Many chemotherapy agents are well-defined, small molecules that typically lead to nonspecific delivery, rapid blood clearance, and low accumulation in tumors, altogether generating severe side effects for cancer patients.^{5,6} To overcome these limitations, they have been conjugated to tumor-targeting nanocarriers, either covalently or supramolecularly, which in principle enhances drug delivery to the tumor.⁷⁻¹⁸ However, many nanocarriers show comparatively low drug-loading capacity (typically <20%),^{19,20} while the resulting tumor accumulation remains disappointingly low: recent studies showed that a median 0.7% of the administered nanoformulated drug dose ends up in solid tumors.^{20,21} In addition, achieving the reproducible preparation of drug-nanoparticle conjugates is often challenging, which restricts the clinical applications of nanodrugs.

Drug self-delivery systems (DSDS) may solve that issue. They consist of small-molecule drugs that self-assemble into nanostructures without the assistance of dedicated nanocarriers.²² These systems combine the easy preparation of small molecules and the tumor-targeting properties of nanoconjugates, achieving high drug loading efficiency.² They also require supramolecular forces that hold in the complex biological environment of a living animal. DSDS proposed to date relies on a combination of hydrophobic forces, hydrogen bonding, and/or metal-ligand coordination. The so-called “metallophilic interaction” is another kind of supramolecular interaction occurring specifically between d^8 or d^{10} metal centers. It is well known in optoelectronics and material science²³ for its ability to modify the photophysical and photochemical properties of metal compounds; it has also been proposed for biological applications, but only *in vitro* demonstrations have been made.²⁴ Here, we demonstrate with a new light-activated DSDS that the metallophilic interaction survives blood circulation in living mice, leading to self-assembled nanoparticles that show outstanding tumor-targeting and phototherapeutic properties in a human skin melanoma xenograft.

Synthesis and characterization of a light-sensitive DSLS.

The **PdL** small molecule (Figure 1a) contains, as in the padeliporfin photosensitizer recently approved for PDT,²⁵ a palladium(II) metal center. In contrast with padeliporfin, however, **PdL** is a bis-cyclometalated palladium compound characterized by the presence of two Pd-C covalent bonds (see Figure 1b and full characterization in Figure S3-S4 and Table S1). Its X-ray structure (Figure 1b) shows head-to-tail dimers with a short interplanar distance of 3.4 Å and a short Pd...Pd distance of 3.518 Å, characteristic of metallophilic interactions. A DFT model of the supramolecular dimer converged at a Pd...Pd distance of 3.52 Å (Figure 1c), matching well with that observed in the crystal. The metallophilic interaction derives from the hybridization of both palladium d_{4z^2} orbitals and π orbitals of the aromatic ligand in the HOMO of the dimer. Meanwhile, TDDFT calculations confirmed the decrease in the HOMO-LUMO gap induced by supramolecular dimerization, with a bathochromic shift of the lowest-energy absorption band from 383 nm for the monomer to 502 nm for the dimer (Figure 1d).

When dissolved in DMSO, **PdL** showed a modest absorption in the 434-540 nm region, an absorption maximum at 481 nm, a concentration-independent emission maximum (564 nm) and a low phosphorescence quantum yield ($\phi_p = 0.0008$) and lifetime ($\tau = 0.406$ ns) characteristic of the monomer (Figure 1e, Table S6). However, in a DMSO:H₂O 1:9 mixture (100 μ M), a rapid (<1 min) increase in the baseline and the generation of a new absorbance peak at 504 nm were observed (Figure 1f), which are typical for metal-metal-to-ligand charge transfer (MMLCT) excited states induced by Pd...Pd interactions²⁶ and altogether suggest self-assembly. This hypothesis was confirmed by TEM images showing nanorods and nanocubes (Figure 1f, insert). Usually, the formation of Pd...Pd supramolecular bonds is accompanied by a long-wavelength emission peak,²⁶ and indeed, an increase in the H₂O content in DMSO:water mixtures ($fw = V_{\text{water}}/V_{\text{total}}$) led to a gradual replacement of the monomeric emission peak at 564 nm (as observed in pure DMSO, $fw = 0.0$) by new emission maxima at 593 nm ($fw = 0.5$) and finally 610-670 nm ($fw = 0.9$) concomitant with the formation of a precipitate (Figure 1g). In THF/H₂O solutions, similar self-assembly was observed, though with slower polymerization rates and different morphologies (Figure S6-S7). Overall, **PdL** appeared as a self-assembling molecule, at least in mixtures of water and organic solvents.

The self-assembly of **PdL** was then studied in a cell-growing medium called Opti-MEM complete that contained 2.5 vol% fetal calf serum (FCS). At 25 μ M, aggregation immediately occurred, as shown by a hydrodynamic diameter of approximately 164 nm determined by dynamic light scattering (DLS, Figure 2a). After 30 min, the maximum hydrodynamic diameter had only slightly shifted to 190 nm, but the number of particles had increased significantly (Figure 2b). The absorption of the solution (Figure 2c) showed a gradual baseline increase during the first 2 h, which is characteristic of light scattering by nanoparticles, to remain constant over 24 h. The main nanostructures observed by TEM in the medium were nanodots (Figure 2d), but these nanodots self-assembled as regular nanofibers that gradually lengthened. Cryo-EM imaging confirmed the formation of nanofibers in such medium, characterized by a well-ordered structure at a repeating distance of ~ 1.68 nm in the Fourier transform image (Figure 2e).

Overall, in cell-growing medium, DLS, EM, and UV-vis spectroscopy demonstrated the time-dependent self-assembly of **PdL** into nanorods and nanoparticles, which, considering DFT and crystal structure analysis, must involve metallophilic Pd...Pd interactions.

In the next step, the influence of self-assembly on the photochemical properties of **PdL** was considered. Photodynamic effects may occur either *via* a type I mechanism (electron transfer) or a type II (energy transfer) mechanism.²⁷ Direct detection of the near-infrared emission peak of $^1\text{O}_2$ at 1270 nm under blue light irradiation (450 nm) was only possible in CD_3OD , hence for the **PdL** monomer. The corresponding $^1\text{O}_2$ generation quantum yield was very low ($\varphi_\Delta = 0.09$, Figure 2f and Table S6). In Opti-MEM medium, hence for the self-assembled form of **PdL** (25 μM), indirect $^1\text{O}_2$ detection using the chemoselective chemical probe 9,10-anthracenediyl-bis(methylene)-dimalonic acid (ABMDMA) showed no decrease in the absorbance band at 378 nm upon green light irradiation, characteristic of the $^1\text{O}_2$ adduct (Figure 2g),²⁸ indicating negligible $^1\text{O}_2$ generation ($\varphi_\Delta = 0.04$, Figure S8).²⁹ Overall, **PdL** is a poor PDT type II sensitizer, both as a monomer in methanol and as aggregates in medium. By contrast, type I PDT sensitizers can be characterized by the initial generation of superoxide radicals ($\text{O}_2^{\cdot-}$), which can further generate other ROS such as HO^\cdot or H_2O_2 .³⁰ When a DMSO or Opti-MEM solution of **PdL** (25 μM) was irradiated with green light in the presence of dihydroethidium (DHE), a chemoselective chemical probe for superoxide, the oxidation product 2-hydroxyethidium was produced efficiently, as shown by its emission at 590-620 nm (Figure 2h, Figure S9).³¹ These results demonstrated that **PdL** is capable of photochemically generating superoxide both in the monomeric and aggregated states, which suggested that as light-activated DSDS, it would behave as a PDT type I photosensitizer.

Biological properties *in vitro* and *in vivo*. Considering the significant absorption of **PdL** at 520 nm ($\epsilon = 915 \text{ M}^{-1} \text{ cm}^{-1}$ in DMSO) and its PDT type I properties, its cytotoxicity was evaluated first *in vitro* using 2D monolayers of lung carcinoma (A549), epidermoid carcinoma (A431), and skin melanoma (A375) cell lines, both in the dark and under green light irradiation. **PdL** showed moderate dark cytotoxicity ($\text{EC}_{50} > 10 \mu\text{M}$) for the three cancer cell lines under normoxic (21% O_2) and hypoxic (1% O_2) conditions (Table S7). By contrast, upon green light irradiation (520 nm, 13 J/cm^2) under normoxia and hypoxia, **PdL** exhibited high phototoxicity with submicromolar EC_{50} and high photoindexes ($\text{PI} = \text{EC}_{50, \text{dark}}/\text{EC}_{50, \text{light}}$) of 32-72 (Figure 3a, Figure S10 and Table S7), thus demonstrating outstanding PDT efficacy even at low dioxygen concentrations. Clearly, at the concentrations used (0.5 and 2 μM), **PdL** showed no or limited cell death in dark conditions, as determined by Annexin V/propidium iodide double staining experiments (Figure 3b and S11). In the light-irradiated group, no toxicity was observed after 2 h, but after 4 h and 24 h, the number of apoptotic and necrotic cells increased significantly, suggesting that **PdL** induced cancer cell death 4 h after irradiation *via* both cell death mechanisms. The cytotoxicity of **PdL** in 3D multicellular tumor spheroid models (A549 and A375), which better mimic the physical penetration of light and drugs in three dimensions,³² was nearly 100-fold higher under light irradiation ($\text{EC}_{50} \sim 0.20 \mu\text{M}$) than under dark conditions ($\text{EC}_{50} > 25 \mu\text{M}$), while light activation was accompanied by the visible collapse of the spheroid cores and dramatic shrinkage of the spheroid diameters (Figure 3c, S12 and Table S7). A further

Hoechst 33342/propidium iodide double-staining experiment was carried out to compare the morphology and health status of A375 spheroids after treatment. The red fluorescence of propidium iodide significantly increased in the green light-irradiated group compared with the dark group (Figure 3c), confirming drug penetration and light-induced cell killing by membrane disruption in 3D environments. Overall, these excellent photocytotoxicity results suggested further *in vivo* testing in mouse tumor models.

Human skin melanoma is known to be prone to resist PDT type II treatment by a combination of a hypoxic tumor microenvironment³³ and melanin-induced quenching of reactive oxygen species (ROS).³⁴ **PdL** was hence evaluated *in vivo* using human skin melanoma (A375) tumor xenografts in nude mice. Following intravenous tail injection (100 μ L, 420 μ M in DMEM (10% FBS), 0.9 mg/kg), the mice showed constant body weight over 20 days (Figure 3d), and the important organs remained healthy, as determined by H&E staining (Figure S13), suggesting low systemic toxicity at this compound dose. In the dark group, **PdL** showed moderate tumor growth inhibition, but green light irradiation (520 nm, 100 mW/cm², 10 min, 60 J/cm²) performed 12 h after injection of the self-assembled **PdL** strongly inhibited tumor growth (Figure 3e). H&E staining of the irradiated tumors at day 5 revealed that the tumor tissues were dramatically damaged in the **PdL+light** group, while the other groups did not show any remarkable effect; TUNEL staining also demonstrated a decrease in cancer cells in the irradiated tumor and cell killing *via* apoptosis (Figure 3f). Overall, these experiments demonstrated not only that **PdL** showed excellent antitumor efficacy in an A375 melanoma mouse model but also that it showed very low cytotoxicity to healthy organs, highlighting the high potential of **PdL** DSDS for anticancer PDT application.

Uptake, biodistribution, and tumor targeting. The low systemic dark toxicity and high antitumor PDT efficacy of **PdL** stimulated us to check drug uptake *in vitro* and *in vivo* using ICP-MS. The cellular uptake of **PdL** (2 μ M) was found to be time-dependent, with the Pd content in A375 cells increasing from 29 (at 2 h) to 172 ng Pd/million cells (at 24 h, Figure 4a). It was also temperature-dependent, with a reduction of 19 ng Pd/million cells at 4 °C 2 h after treatment (5 μ M) compared to 44 ng Pd/million cells at 37 °C (Figure 4b). Further coincubation experiments (Figure 4b) showed that active internalization occurred *via* clathrin-mediated endocytosis (pitstop) and micropinocytosis (wortmannin). Altogether, these results highlighted that both energy-independent and energy-dependent cellular uptake took place *in vitro*, suggesting that **PdL** may pass through the cell membrane as both isolated molecules and nanoaggregates.

An essential question at this stage was to understand whether the nanoparticles formed by **PdL** in cell-growing medium *in vitro* would also form in a living mouse. Thus, the presence and morphology of nanostructures in the bodies of mice injected with **PdL** were investigated in more detail. First, blood samples taken from the eye socket of mice 5 min after intravenous tail injection of **PdL** showed roughly spherical, high-contrast nanoparticles, characterized by an average size of 181 \pm 75 nm (Figure S14). Similar to those found in the injected DMEM solution, these nanoparticles were rich in palladium according to EDX analysis (Figure 4c-d), which confirmed that they contained **PdL**. Altogether, these results suggested that molecules of **PdL** aggregated into nanoparticles in DMEM and that upon

intravenous injection, they remained self-assembled in blood while circulating. Second, 12 h after tail vein injection of **PdL**, the A375 tumor was sectioned and imaged by EM. These images (Figure 4e, 1 and 0.5 μm scale, indicated by red arrows) showed dark nanosized spots in the cytoplasm of the cancer cells with an average diameter of 260 ± 75 nm, slightly larger than the diameter of nanoparticles in blood. These dark spots were not observed in the untreated control group (Figure S15); thus, we interpret them as palladium-containing nanoparticles. Overall, the presence of nanoparticles both in the blood and in the tumor tissue of mice treated with **PdL** is proof that the Pd...Pd interaction causing the self-assembly of the molecule in medium is strong enough to keep the nanostructures in circulating blood, which leads to delivery of the prodrug to the tumor.

To quantify tumor delivery, the biodistribution of Pd was determined by ICP-MS in A375 mouse xenografts several hours (2, 6, 12, 20, 24 h) after intravenous tail injection of **PdL**. As shown in Figure 4f, the complex showed low accumulation (below $0.27 \mu\text{g/g}$ tissue) in the heart, kidney, and lung, while the liver showed significantly higher accumulation (above $1.0 \mu\text{g}/\text{per gram tissue}$), as expected considering its role in detoxification and metabolism of exogenous substances. Noticeably, the accumulation level of **PdL** in the liver gradually decreased over time. Meanwhile, the tumor tissue showed an increasing Pd accumulation from $0.17 \mu\text{g}$ per gram tissue after 2 h to a peak of $0.87 \mu\text{g}$ per gram tissue at 12 h, which corresponded to an impressive 10.2 %ID/g of the injected drug (Figure 4f and 4g), and finally decreased to $0.17 \mu\text{g}$ per gram tissue at 24 h. These results highlight both the long circulation time and extraordinary tumor accumulation rate of **PdL** nanoparticles, which peak in the tumor at 12 h. In conclusion, **PdL** appears as a particularly well-performing DSDS characterized by an easy synthesis and formulation in biocompatible buffer, a high-drug loading efficiency of the self-assembled nanoparticles, a low systemic toxicity to the tumor-bearing mouse for these nanoparticles, and excellent tumor accumulation and antitumor efficacy upon light irradiation using a drug-to-light interval of 12 h.

Discussion And Conclusion

One main advantage of DSDS is its high drug-loading capacity, as the nanoparticles are mostly composed of drug molecules. However, with traditional DSDS, such high drug-loading capacity may come with high toxicity to blood-filtering organs such as the liver or kidneys,³⁵ as each nanoparticle brings into a cell many toxic molecules. Light-activated DSDSs bring a solution to this problem, as the self-assembling drug only becomes toxic after light irradiation.³⁶ As the liver remains in the dark, high hepatic uptake is not a problem for **PdL**, provided liver clearance occurs, which is suggested in Figure 4f. Light activation hence provides a dramatic advantage compared to traditional DSDSs.

Light-activated DSDSs can also be analyzed from the point of view of photodynamic therapy. Of course, PDT treatment offers a patient-friendly alternative to chemotherapy, with the potential to inhibit tumor proliferation while minimizing side effects by selective light irradiation of tumor tissue.³⁷ However, photosensitizer molecules taken up in healthy tissues also lead to undesired photosensitivity (*e.g.*, skin) for the patient, a typical side effect of PDT with Photofrin.³⁸ It is hence essential that the photosensitizer be delivered with high efficacy to the tumor tissue. Many reports have demonstrated that nanoconjugates

enable an increase in the tumor accumulation of molecular drugs, including PDT photosensitizers.^{39,40} However, the low average drug-loading capacity (typical 20 wt%) and tumor accumulation efficacy (median 0.7% ID) achieved by classical drug delivery nanosystems²⁰ suggested the urgency to develop new drug delivery nanoconjugates, also in the context of PDT.

To our knowledge, no report has addressed the potential of metallophilic interactions for these purposes; in particular, their ability to afford stable nanostructures in living animals, as reported here, is unprecedented. The drug delivery properties of the obtained system are remarkable: the circulation time is long (>12 h), and the drug accumulation of PdL in the tumor tissue is outstanding (up to 10.2% ID/g). Photochemically speaking, unlike porphyrins, the **PdL** complex maintains excellent photodynamic properties in the aggregated state, even in a hypoxic tumor microenvironment. The fact that such results can be obtained at the synthetic cost of a simple, well-defined small molecule raises promising possibilities for real-life clinical applications. With these results in hand, we conclude that the metallophilic interaction has a high potential to build high-performance supramolecular nanocarriers with improved tumor accumulation and that the Pd...Pd interaction observed with complexes such as **PdL** can generate photodynamic systems that conserve their phototoxic properties under hypoxia.

Declarations

Acknowledgments

Prof. E. Bouwman is wholeheartedly acknowledged for scientific discussion and support. Dr. S. Zheng is thanked for ICP-MS measurement. The Cryo-EM measurements benefited from access to The Netherlands Centre for Electron Nanoscopy (NeCEN) at Leiden University.

Funding

China Scholarship Council (CSC) for a personal grant (No. 201606200045) to X.-Q Zhou; European Research Council for a Starting Grant to S. Bonnet; National Natural Science Foundation of China (22022803, 22078046, 21808028) for funding W. Sun; Leiden University for a Huygens Fellowship to P. Papadopoulou.

Author contributions

Conceptualization: XQZ, SB, WS

Methodology: XQZ, PW, VR, SJ, XL, SA, PP, MAS

Calculation : YS, FB, SB

Funding acquisition: WS, SB

Project administration: XQZ, WS, SB

Supervision: WS, SB

Writing – original draft: XQZ, WS, SB

Writing – review & editing: PW, VR, PP, MAS, AK.

Competing interests

The authors declare that they have no competing interests.

Supplementary Materials

Materials and methods; single-crystal X-ray crystallography; DFT and TDDFT calculations of PdL; photophysical properties of PdL; self-assembly of PdL in solvent mixtures; phototoxicity of PdL and cell death mechanism determination in cancer cells; tumor xenograft experiments.

References

1. Siegel, R.L., Miller, K.D. & Jemal, A. Cancer statistics, 2020. *CA Cancer J. Clin.* **70**, 7–30 (2020).
2. Shen, S., Wy, Y., Liu, Y. & Wu, D. High drug-loading nanomedicines: progress, current status, and prospects. *Int. J. Nanomedicine* **12**, 4085–4109 (2017).
3. Chabner, B.A. & Roberts, T.G. Chemotherapy and the war on cancer. *Nat. Rev. Cancer* **5**, 65–72 (2005).
4. Raj, L., *et al.* Selective killing of cancer cells by a small molecule targeting the stress response to ROS. *Nature* **475**, 231–234 (2011).
5. Chen, Z.G. Small-molecule delivery by nanoparticles for anticancer therapy. *Trends Mol. Med.* **16**, 594–602 (2010).
6. Salami, J. & Crews, C.M. Waste disposal—an attractive strategy for cancer therapy. *Science* **355**, 1163–1167 (2017).
7. Zeinali, M., *et al.* Nanovehicles for co-delivery of anticancer agents. *Drug Discov. Today* **25**, 1416–1430 (2020).
8. Nam, J., *et al.* Cancer nanomedicine for combination cancer immunotherapy. *Nat. Rev. Mater.* **4**, 398–414 (2019).
9. Pottanam Chali, S. & Ravoo, B.J. Polymer Nanocontainers for Intracellular Delivery. *Angew. Chem. Int. Ed.* **59**, 2962–2972 (2020).
10. Cheng, Z., Al Zaki, A., Hui, J.Z., Muzykantov, V.R. & Tsourkas, A. Multifunctional nanoparticles: cost versus benefit of adding targeting and imaging capabilities. *Science* **338**, 903–910 (2012).
11. Kranz, L.M., *et al.* Systemic RNA delivery to dendritic cells exploits antiviral defence for cancer immunotherapy. *Nature* **534**, 396–401 (2016).
12. Kaspler, P., *et al.* A ruthenium(ii) based photosensitizer and transferrin complexes enhance photophysical properties, cell uptake, and photodynamic therapy safety and efficacy. *Photochem.*

- Photobiol. Sci.* **15**, 481–495 (2016).
13. Sun, W., *et al.* An Amphiphilic Ruthenium Polymetallo drug for Combined Photodynamic Therapy and Photochemotherapy In Vivo. *Adv. Mater.* **29**, 1603702 (2017).
 14. Miller, J.W., *et al.* Photodynamic Therapy of Experimental Choroidal Neovascularization Using Lipoprotein-Delivered Benzoporphyrin. *Arch. Ophthalmol.* **113**, 810–818 (1995).
 15. Solban, N., Rizvi, I. & Hasan, T. Targeted photodynamic therapy. *Lasers Surg. Med.* **38**, 522–531 (2006).
 16. Youssef, Z., *et al.* New Targeted Gold Nanorods for the Treatment of Glioblastoma by Photodynamic Therapy. *J. Clin. Med.* **8**(2019).
 17. Karges, J., Díaz-García, D., Prashar, S., Gómez-Ruiz, S. & Gasser, G. Ru(II) Polypyridine Complex-Functionalized Mesoporous Silica Nanoparticles as Photosensitizers for Cancer Targeted Photodynamic Therapy. *ACS Appl. Bio Mater.* **4**, 4394–4405 (2021).
 18. Karges, J., Li, J., Zeng, L., Chao, H. & Gasser, G. Polymeric Encapsulation of a Ruthenium Polypyridine Complex for Tumor Targeted One- and Two-Photon Photodynamic Therapy. *ACS Appl. Mater. Interfaces* **12**, 54433–54444 (2020).
 19. Greenwald, R.B., Choe, Y.H., McGuire, J. & Conover, C.D. Effective drug delivery by PEGylated drug conjugates. *Adv. Drug Deliv. Rev.* **55**, 217–250 (2003).
 20. Wilhelm, S., *et al.* Analysis of nanoparticle delivery to tumours. *Nat. Rev. Mater.* **1**, 1–12 (2016).
 21. Dai, Q., *et al.* Quantifying the Ligand-Coated Nanoparticle Delivery to Cancer Cells in Solid Tumors. *ACS Nano* **12**, 8423–8435 (2018).
 22. Qin, S.Y., Zhang, A.Q., Cheng, S.X., Rong, L. & Zhang, X.Z. Drug self-delivery systems for cancer therapy. *Biomaterials* **112**, 234–247 (2017).
 23. Yam, V.W.-W., Au, V.K.-M. & Leung, S.Y.-L. Light-Emitting Self-Assembled Materials Based on d8 and d10 Transition Metal Complexes. *Chem. Rev.* **115**, 7589–7728 (2015).
 24. Mauro, M., Aliprandi, A., Septiadi, D., Kehr, N.S. & De Cola, L. When self-assembly meets biology: luminescent platinum complexes for imaging applications. *Chem. Soc. Rev.* **43**, 4144–4166 (2014).
 25. Azzouzi, A.-R., *et al.* Padeliporfin vascular-targeted photodynamic therapy versus active surveillance in men with low-risk prostate cancer (CLIN1001 PCM301): an open-label, phase 3, randomised controlled trial. *Lancet Oncol.* **18**, 181–191 (2017).
 26. Zou, C., *et al.* Palladium(ii) N-heterocyclic allenylidene complexes with extended intercationic PdPd interactions and MMLCT phosphorescence. *Chem. Commun.* **54**, 5319–5322 (2018).
 27. Baptista, M.S., *et al.* Type I and Type II Photosensitized Oxidation Reactions: Guidelines and Mechanistic Pathways. *Photochem. Photobiol.* **93**, 912–919 (2017).
 28. Karges, J., *et al.* Rationally Designed Long-Wavelength Absorbing Ru(II) Polypyridyl Complexes as Photosensitizers for Photodynamic Therapy. *J. Am. Chem. Soc.* **142**, 6578–6587 (2020).
 29. Zhou, X.Q., *et al.* The Self-Assembly of a Cyclometalated Palladium Photosensitizer into Protein-Stabilized Nanorods Triggers Drug Uptake In Vitro and In Vivo. *J. Am. Chem. Soc.* **142**, 10383–10399

- (2020).
30. Monro, S., *et al.* Transition Metal Complexes and Photodynamic Therapy from a Tumor-Centered Approach: Challenges, Opportunities, and Highlights from the Development of TLD1433. *Chem. Rev.* **119**, 797–828 (2019).
 31. Peshavariya, H.M., Dusting, G.J. & Selemidis, S. Analysis of dihydroethidium fluorescence for the detection of intracellular and extracellular superoxide produced by NADPH oxidase. *Free Radic. Res.* **41**, 699–712 (2007).
 32. Friedrich, J., Seidel, C., Ebner, R. & Kunz-Schughart, L.A. Spheroid-based drug screen: considerations and practical approach. *Nat. Protoc.* **4**, 309–324 (2009).
 33. O'Connell, M.P., *et al.* Hypoxia induces phenotypic plasticity and therapy resistance in melanoma via the tyrosine kinase receptors ROR1 and ROR2. *Cancer Discov.* **3**, 1378–1393 (2013).
 34. Herrling, T., Jung, K. & Fuchs, J. The role of melanin as protector against free radicals in skin and its role as free radical indicator in hair. *Spectrochim. Acta A Mol. Biomol. Spectrosc.* **69**, 1429–1435 (2008).
 35. Bartucci, R., Paramanandana, A., Boersma, Y.L., Olinga, P. & Salvati, A. Comparative study of nanoparticle uptake and impact in murine lung, liver and kidney tissue slices. *Nanotoxicology* **14**, 847–865 (2020).
 36. Brown, S.B., Brown, E.A. & Walker, I. The present and future role of photodynamic therapy in cancer treatment. *Lancet Oncol.* **5**, 497–508 (2004).
 37. McFarland, S.A., Mandel, A., Dumoulin-White, R. & Gasser, G. Metal-based photosensitizers for photodynamic therapy: the future of multimodal oncology? *Curr. Opin. Chem. Biol.* **56**, 23–27 (2020).
 38. Moriwaki, S.I., *et al.* Analysis of photosensitivity in Japanese cancer-bearing patients receiving photodynamic therapy with porfimer sodium (PhotofrinTM). *Photodermatol. Photoimmunol. Photomed.* **17**, 241–243. (2001).
 39. Salvioni, L., *et al.* Thirty Years of Cancer Nanomedicine: Success, Frustration, and Hope. *Cancers* **11**(2019).
 40. Yu, Z., Zhou, P., Pan, W., Li, N. & Tang, B. A biomimetic nanoreactor for synergistic chemiexcited photodynamic therapy and starvation therapy against tumor metastasis. *Nat. Commun.* **9**, 5044 (2018).

Figures

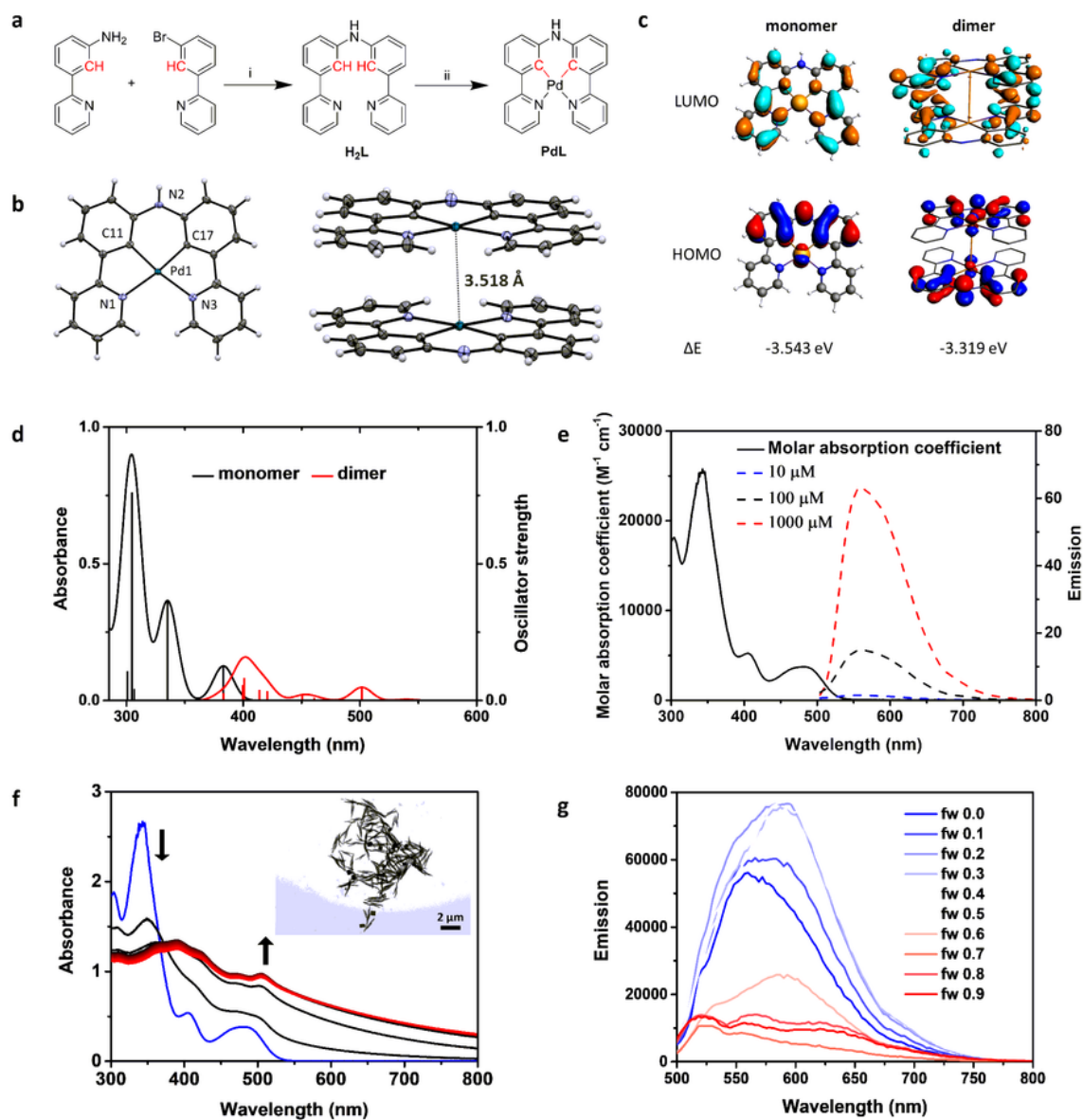


Figure 1

Synthesis, crystal structure, DFT calculation and photophysical properties of **PdL**. (a) Synthesis of H_2L and **PdL** ((i) $Pd(dba)_2$, $KOt-Bu$, BINAP, toluene, 95 °C, N_2 , 72 h, yield 67%; (ii) $Pd(OAc)_2$, CH_3COOH , 135 °C, 24 h, yield 56%). (b) Displacement ellipsoid plot (50% probability level) of **PdL** and its stacking structure at 110(2) K. (c) DFT calculation of HOMOs (bottom) and LUMOs (top) orbitals of **PdL** as a monomer or dimer (calculated Pd...Pd distance 3.52 Å). Occupied orbitals (HOMO) have red and blue lobes, and

unoccupied orbitals (LUMO) have brown and cyan lobes. Element color code: blue = N, gray = C, brown = Pd, white = H. (d) TDDFT-calculated spectra of **PdL** as a monomer (red line) or dimer (black line). Level of theory: TDDFT/PBE0/TZP/COSMO (methanol). (e) The absorption spectrum (black solid line) and emission spectra of **PdL** in pure DMSO solution at different concentrations (blue dashed line 10 μM ; black dashed line 100 μM , red dashed line 1000 μM ; excitation 419 nm). (f) Time evolution of the absorption spectra of DMSO/H₂O solution (100 μM , V/V = 1/9) of **PdL** at 298 K for 30 min (30 s interval, the color of spectra change from black (0 min) to red (30 min)); the blue line is the absorbance spectra of **PdL** (100 μM) in pure DMSO. Inset picture: TEM images of nanostructures of **PdL** in DMSO/H₂O solution (100 μM , V/V = 1/9, scale bar 2 μm). (g) Emission spectra of **PdL** (100 μM) in H₂O/DMSO mixtures with different volumetric ratios ($f_w = V_{\text{water}}/V_{\text{total}}$).

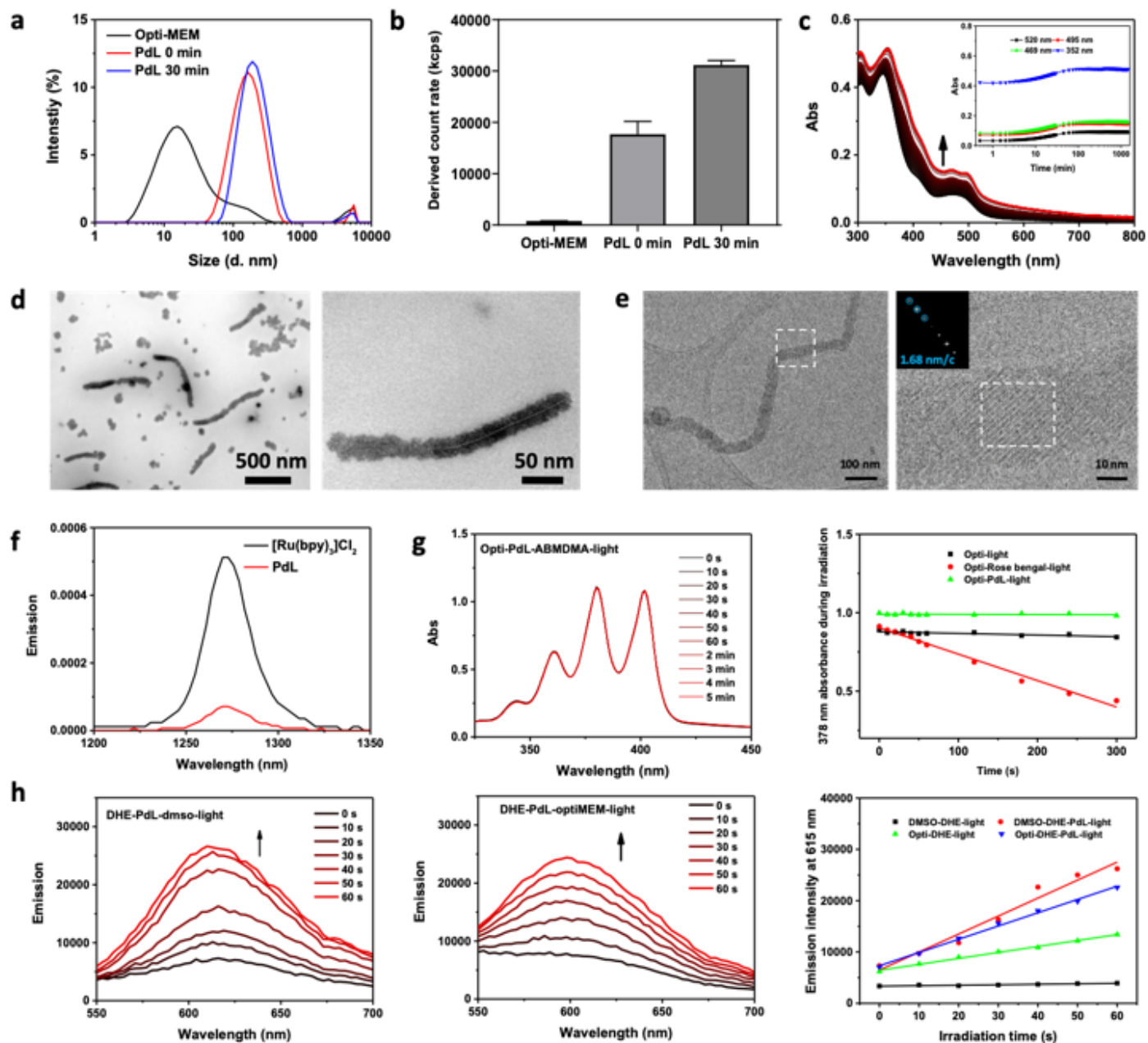


Figure 2

Self-assembly and aggregation nanostructure of **PdL** in cell medium. (a) Size distribution of Opti-MEM complete medium and its **PdL** (25 μ M) solution at 0 min (red line) or 30 min (blue line) according to DLS analysis at room temperature. (b) DLS-derived count rate of **PdL** solution in Opti-MEM complete medium for 0 and 30 min. (c) Observation of absorbance spectra of **PdL** (25 μ M) in Opti-MEM complete medium over 24 h (30 s interval for the first 30 min, 15 min interval for the next 23.5 h). (d, e) TEM images and cryo-EM images of samples prepared from an Opti-MEM complete medium solution of **PdL** (25 μ M) at room temperature. (f) Singlet oxygen emission spectra of [Ru(bpy)₃]Cl₂ (black) and **PdL** (red) in CD₃OD irradiated with blue light ($\lambda_{\text{ex}} = 450$ nm, 50 mW, 0.4 W/cm²). (g) The absorbance change of ABMDMA Opti-MEM complete solution (100 μ M) in the presence of **PdL** (25 μ M) under green light irradiation (515

nm, 2.0 mW) over 5 min. (h) The emission spectra of a dihydroethidium (DHE) solution (DMSO or Opti-MEM complete) in the presence of **PdL** (25 μ M) under green light irradiation (515 nm, 2.0 mW) over 60 s.

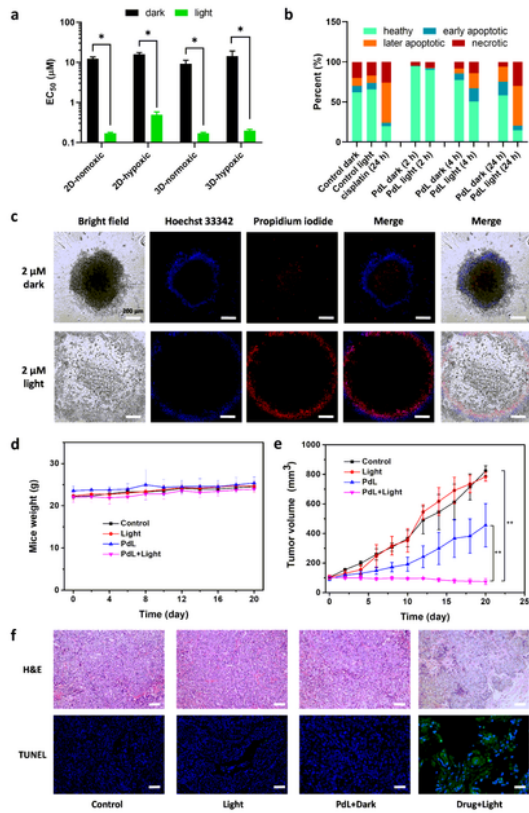


Figure 3

The *in vitro* and *in vivo* anticancer properties of **PdL**. (a) EC_{50} values of **PdL** to A375 2D-monolayer and 3D-spheroid cancer cells incubated, either in the dark or upon green light irradiation (13 J/cm^2), and in normoxic or hypoxic conditions; statistical significance was set to $p < 0.05$ (*). (b) Flow cytometry quantification of healthy, early apoptotic, later apoptotic and necrotic A375 cells after treatment with **PdL** ($2 \text{ }\mu\text{M}$) in the dark or with green light irradiation in a time gradient (2 h, 4 h, 24 h). Cisplatin ($7.5 \text{ }\mu\text{M}$, 24 h) was used as a positive control. (c) Confocal images of 3D-normoxic A375 spheroids (scale bar 200 nm) in the dark or green light irradiation, with Hoechst 33342/propidium iodide double staining after treatment with **PdL** ($2 \text{ }\mu\text{M}$) for 72 h. (d) Time evolution of the mouse weight 20 days posttreatment. (e) A375 tumor growth inhibition in different mouse groups treated by tail intravenous injection. Statistical significance was set to $p < 0.01$ (**). Light irradiation conditions: 520 nm, 100 mW/cm^2 , 10 min, 60 J/cm^2 . Dose: $2.1 \text{ }\mu\text{mol/kg}$, $420 \text{ }\mu\text{M}$, $100 \text{ }\mu\text{L DMEM}$ (10% FBS), 0.9 mg/kg . (f) H&E and TUNEL staining assay of tumor slices of mice in different groups at day 5 (scale bar 200 mm).

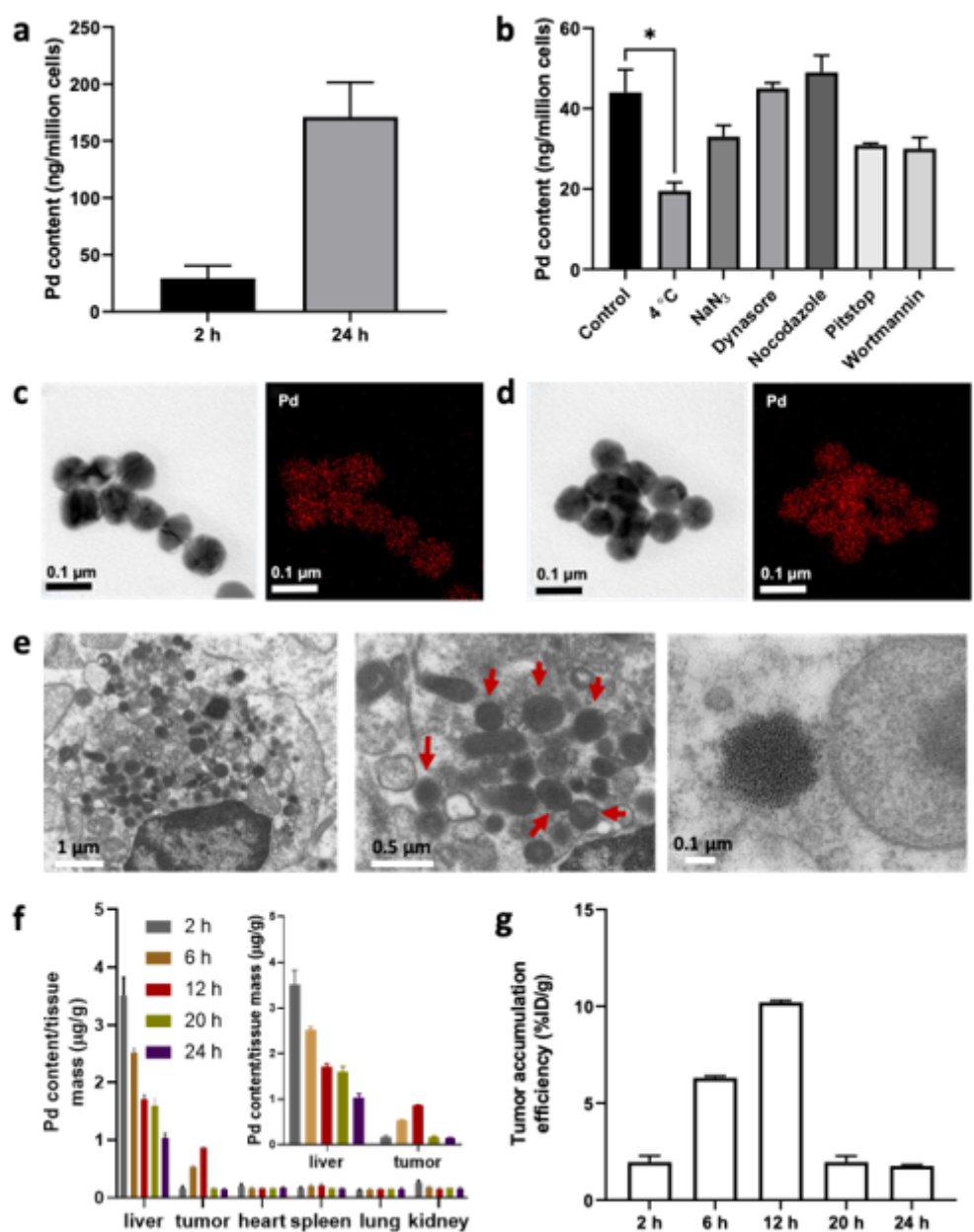


Figure 4

Cellular uptake *in vitro* and biodistribution, nanoparticle morphology and Pd content, and tumor accumulation of **PdL** *in vivo* in mouse A375 tumor xenografts. The Pd content (ICP-MS) of A375 skin melanoma cell monolayers (a) 2 or 24 h after treatment with **PdL** (2 μ M) and (b) 2 h after treatment with **PdL** (5 μ M) in combination with different uptake inhibitors. (c, d) TEM and EDX images of nanoparticles detected in DMEM (10% FBS) and in the blood of mice 5 min after treatment with **PdL**. (e) EM images at different magnifications of slices of A375 tumors in mouse xenografts 12 h after intravenous tail injection of **PdL**. Nanoparticles are indicated by red arrows. (f) Biodistribution of palladium (ICP-OES) in different organs of mice at different time points after intravenous tail injection of **PdL**. (g) Tumor palladium accumulation efficiency in mice at different time points after intravenous tail injection by **PdL**.

$\%ID/g = (\text{Pd content of tumor}/\text{Pd content of injection solution}) \times 100\% / \text{mass of measured organs}$). *In vivo* injection conditions: 2.1 $\mu\text{mol}/\text{kg}$, 420 μM , 100 μL DMEM (10% FBS), 0.9 mg/kg .

Supplementary Files

This is a list of supplementary files associated with this preprint. Click to download.

- [PdLxraycheckcif.pdf](#)
- [PdLxray.cif](#)
- [zhouNatureChemistryESI.pdf](#)